A novel wheel-type vibration-magnetorheological compound finishing method

Yan Gu [1, 2,*]•Bin Fu [1, 2]•Jieqiong Lin [1, 2,*]•Xiuyuan Chen [3]•Weidong Zhou [1, 2]•Bingjin Yu [1, 2]•Huibo Zhao[1, 2]•Zhen Li [1, 2]•Zisu Xu[1, 2]

Abstract

Magnetorheological finishing (MRF) is an important technique to achieve the surface precision of difficult-to-cut materials. In this paper, a wheel-type vibration-magnetorheological compound finishing is proposed in terms of reducing the unidirectional scratch caused by the wheel type magnetorheological finishing tool and further improving the convergence rate of surface roughness. The vibration-magnetorheological coupling was realized through utilizing designed magnetorheological finishing (MRF) wheel and a nonresonant vibrational device (NRVD). Through the theoretical and experimental analysis, the surface roughness has been verified improved through increasing the normal and tangential forces, which are associated with introducing 2D vibration. The flow and viscoelastic models of the MRP fluid were established based on hydrodynamic lubrication and viscoelasticity theories. Finally, the feasibility of the proposed finishing method was verified by the results of improving surface roughness through designing reasonable processing experiment.

[1] Jilin Provincial Key Laboratory of Micro-Nano and Ultra-Precision Manufacturing, School of Mechatronic Engineering, Changchun University of Technology, Yan'an Ave 2055, Changchun, Jilin 130012, PR China;

[2] Jilin Province Key Laboratory of International Science and Technology Cooperation for High Performance Manufacturing and Testing , School of Mechatronic Engineering， Changchun University of Technology, Yan'an Ave 2055, Changchun, Jilin 130012, PR China;

[3] Centre for Precision Manufacturing, DMEM, University of Strathclyde, Glasgow, G1 1XQ, UK.4

* E-mail: guyan@ccut.edu.cn (Y.G.); linjieqiong@ccut.edu.cn (J.Q.L.).

Tel: +86-431-8571-6288.

Nomenclature			
R	radius of the MRF wheel	ϕ_s	volume percentage of hexametaponate
h_1	thickness of the belt	τ	shear stress of the MRP fluid
h_0	minimum working gap	τ_0	shear yield stress of the MRP fluid
D	immersion depth of the belt	η_1	off-state viscosity of the MRP fluid
L	length of finishing zone	$\dot{\gamma}$	shear rate
W	effective width generated by a belt	H	magnetic field intensity
S	finishing zone boundary	μ_0	space permeability
B	magnetic flux density in the finishing zone	M_s	saturation magnetic field of the magnetic particles
h	working gap	η_0	viscosity of the base fluid
ϕ_w	volume percentage of water	E	ideal spring stiffness
ϕ_C	volume percentage of CI particles	η_2	ideal Newtonian fluid viscosity
ϕ_a	volume percentage of abrasive	G^*	complex shear modulus
ϕ_n	volume percentage of nano-silica	G_1	real part of the complex shear modulus
ϕ_g	volume percentage of glycerol	G_2	imaginary part of the complex shear modulus

F_N	normal force
P_N	normal stress
P_d	hydrodynamic pressure
P_m	magnetization pressure
μ_f	magneto conductivity of the water
μ_p	magneto conductivity of magnetic particle
h_{m0}	corrected minimum gap
h_a	corrected working gap
A_1	amplitude of the sample moves harmonically along the X-axis
f_1	frequency of the sample moves harmonically along the X-axis
U_1	linear velocity of the sample surface along the X-axis
ω	rotates angular velocity of the finishing wheel
U_2	linear velocity near the finishing wheel
$\bar{P}_d$	dimensionless pressure
τ_X	X-axis shear stress
dp_d/dx	pressure gradient
$\tau_1(x,z)$	steady shear stress distribution
τ_1	steady shear stress
γ_x	X-axis oscillatory shear strain
τ_2	X-axis oscillatory shear stress
F_X	X-axis tangential force
A_2	amplitude of the sample moves harmonically along the Y-axis
f_2	frequency of the sample moves harmonically along the Y-axis
γ_Y	Y-axis oscillatory shear strain
τ_Y	Y-axis shear stress
F_Y	Y-axis tangential force
$\overline{F_N}$	theoretical value of the normal force in one period
$\overline{F_X}$	theoretical value of the X-axis tangential force in one period
$\overline{F_Y}$	theoretical value of the Y-axis tangential force in one period
T	period of vibration

1 Introduction

Difficult-to-cut materials, especially for engineering ceramics, have received much attention in academic and industrial areas as the inherent superior properties of high specific stiffness, chemical stability, and wear resistance.

Currently, they serve the key part in multiple applications such as medical devices, optics, and microelectronics [1]. Targeting at withstanding extreme working environments and specific task requirements, kinds of components (such as artificial implants [2], silicon carbide (SiC) galvanometer mirror [3], electronic packaging ceramic substrate [4].) not only need enough strength to meet the reliability，but also require maintain the ultra-precision surface/subsurface integrity. It has been commonly recognized that polishing is the final and critical step to achieve ultra-smooth and even non-damage surface after former procedures of turning, grinding or other moulding processes [5]. The main objective is to remove the micro surface/subsurface damage generated by the abrasive grains or diamond tool tip related to the brittle fracture property [6]. Based on the current investigations and publications from scholars and researchers around the world, magnetic field-assisted finishing (MFAF), a promised finishing technology, can effectively remove existing defects on the workpiece surface without forming new damage in the aspect of hard and brittle materials ultra-precision machining [7]. The current MFAF technologies mainly include magnetic abrasive finishing (MAF) [8-10], magnetic composite fluid polishing (MCFP) [11], and magnetorheological finishing (MRF). It is one of the important research directions in ultraprecision machining to realize the machining of difficult-to-cut materials by using MRF technology [12].

It is an important factor to affect processing performance for a MRF method that relative motion between the polishing tool and the workpiece. The surface quality can be improved through complicating their relative movement. Wang et al. [13] found that traditional grid and spiral tool paths have limited effects on the improvement of the unidirectional scratches in the MRF based on a wheel tool. Their solution is making the wheel tool rotate around the axis perpendicular to the workpiece surface. The directional micro- scratches are reduced by continuously changing the shear flow direction of the MRP fluid. Paswan et al. [14] developed a novel magnetorheological honing head and demonstrated the counter-rotating motion of the workpiece significantly extends the motion path length of the abrasive particles and reduces the helix angle, which further smooths the peaks and valleys of the targeted surface. To overcome the negative effects of centrifugal force on the material removal efficiency and surface quality, Jung et al. [15] employed the slider-crank mechanism to drive the specimen via fast linear reciprocating motion. The surface roughness of the sample is improved by 193% verifing the feasibility of applying technology. Based on driving the tool or machined workpiece to generate targeted motion with controlled amplitude and frequency, vibration-assisted machining (VAM) has been introduced into the MFAF technologies for surface finishing. Most of VAM technologies operated at resonant and non-resonant

modes [16]. The advantages of them are producing higher energy at the short period of time and work at the flexible frequency range, respectively. Guo et al. [17] introduced the local vibration-assisted magnetic polishing method based on the mechanism of driving the magnetic abrasives to scan an S-curve on the microstructure surface targeted at reducing the revolution turning scratches. Misra et al. [18] superimposed the ultrasonic vibration on the workpiece to facilitate magnetic abrasive finishing through increasing covered area of the abrasive particle to enhance the material removal rate. Jiang et al. [19] applied an one-dimensional ultrasonic vibration which parallel to the direction of wheel speed on the workpiece and the surface quality of MRF based on a wheel tool is improved. Zhang et al. [20] proposed the ultrasonic-magnetorheological composite finishing method. An ultrasonic vibration perpendicular to the direction of tool rotation is superimposed and the energy generated by the vibration improves the finishing quality and efficiency of MRF. Compare to limitation working frequency of the resonant vibrational device [21], non-resonant vibration system based on flexure hinge extends the operating modes. And it has been widely used, such as fast tool servo turning, vibration assisted milling and vibration assisted polishing [22-24]. Li et al. [25] developed a new non-resonant vibration assisted polishing head, which can generate complex Lissajous polishing trajectory by controlling amplitude and frequency. The trajectory not only improves material removal rate but also reduces periodic polishing marks. Gu and Kang et al. [26, 27] proposed the non-resonant vibration-assisted magnetorheological polishing method based on the two-dimensional non-resonant vibration and permanent magnet polishing head. The additional impact tangential force generated by the vibration acting on abrasive particles not only significantly reduces the surface roughness but also increases the material removal rate. Based on the above literature review, it can be found that it is feasible to improve the surface finish of MFAF by introducing nonresonant vibration. So, it was proposed and verified in this paper that a method using micron 2D vibration to reduce unidirectional scratches and improve machining uniformity of wheel-type MRF. To the authors' knowledge, no attempt has been made to combine the MRF based on a wheel tool with two-dimensional non-resonant vibration to develop a new polishing method.

The finishing force is the core factor for analyzing the processing mechanism of a MRF method. Sidpara et al. [28, 29] quantitated the material removal rate, surface roughness, processing heat, and residual stress of wheel-type MRF based on calculating the force on the effective abrasives. Their research shows the importance of polishing force study. The difficulty of MRF mechanical modeling lies in clearing fluid flow behavior and quantifying the rheological properties of the MRP fluid [30]. Kordonski et al. [31] used Bingham model to describe the rheological characteristics of MRP fluid and fluid dynamic pressure lubrication theory to establish a one-dimensional fluid flow model of MRF based on a wheel tool. Their calculations of normal and tangential forces based on the stress distribution agreed well with the measurements. Chen et al. [32] improved the Bingham model to describe unyielding MRP fluids. Based on this model, they established a three-dimensional fluid flow model of MRF based on a small ball-end permanent magnet polishing head for obtaining the shear stress distribution on the workpiece surface. The measurement results of material removal depth and polishing spot shape verify the accuracy of shear stress distribution. Xu et al. [33] refined surface roughness convergence rate of the cluster magnetorheological finishing (CMRF) method by filling the MRP fluid into the pores of the porous foam to increase normal force. They established the fluid flow model by analyzing the influence of porous foam on the thickness of polishing film and explained that the mechanism of increasing normal force. Zhang et al. [34] used laser energy to heat the MRP fluid at the entrance of the polishing zone, aiming at reducing viscosity to solve the problem of MRP fluid accumulation. Based on heat transfer theory and experiment, the function between viscosity of the MRP fluid and temperature was established. The shear force and hydrodynamic pressure model of polishing zone are established on this basis, and the basic principle of heat flow coupling effect is revealed. Zhang et al. [35] calculated acoustic pressure based on the propagation velocity and attenuation coefficient of the ultrasonic wave in MRP fluid. The mechanism revealed ultrasonic vibration can improve the normal force and material removal rate. Moreover, Zhai et al. [36] found that vertical ultrasonic vibration not only affects the normal force, but also changes the tangential force in terms of ultrasonic vibration-assisted MRF. The effect of ultrasonic vibration on the normal and tangential force was explained by calculating the effective abrasive acceleration and the time of MRP fluid disengaging from the workpiece. However, the precision machining method developed in this paper is quite different from the traditional MRF. Two-dimensional non-resonant vibration causes MRP fluid in the machining area to flow under the compound action of steady and oscillatory shear. Thus, the fluid flow models of existing MRF methods are not applicable. In addition, the existing ultrasound vibration assisted MRF model cannot explain the influence of two-dimensional non-resonant vibration on the rheological characteristics and flow state of MRP fluid.

In order to solve the research gaps in the above aspects, the finishing force model of the proposed WVMCF is investigated based on the modified flow and rheological property models of the MRP fluid. Furthermore, the operational principle that 2D vibration reduces scratches and improves surface finish is investigated based on the

finishing force model. The remainder of this paper is organized as follows. The principle of WVMCF is introduced in Section 2. The mechanical behaviour of WVMCF is theoretically investigated in Section 3. The experimental setup and process parameters are introduced in Section 4, where pressureless sintered silicon carbide ceramics ceramic, which is a typically hard and brittle material, is selected as the sample material. The effect of amplitudes and frequencies on surface quality is respectively discussed by analysing the finishing forces and experiment results in Section 5.

2 Working principle of the WVMCF

The schematic diagram of the proposed WVMCF method is shown in Fig. 1. Key parts served in this method include a new magnetorheological finishing wheel (MRF wheel) and a nonresonant vibrational device (NRVD). The motion along the X-axis of the MRF wheel and the motion along Y-axis of the NRVD adjust the position of the finishing zone. And the motion along the Z-axis of the MRF wheel adjusts the working gap. So, the entire sample surface can be polishing by the method. Besides, the 2D vibration is achieved by the NRVD drives the targeted sample at the designed amplitude and frequency. As shown in Fig. 1b, the MRP fluid can be attached on the four finishing belts of the wheel. Four polishing points are produced on the surface when the belts contact the sample. So, the novel MRF wheel presented in this paper is equivalent to four traditional wheel-type MRF tools in parallel. The four points were named as the finishing zone. The steady shear flow driven by the finishing belts is coupled with the oscillating shear flow generated by planar vibration to form a composite shear flow. And the composite shear flow generates greater normal force (F_N) and significantly increases the tangential force (F_X) and the tangential force (F_Y) along X and Y axes, respectively. Accordingly, increasing the finishing forces improves the ability of abrasive particles to remove surface roughness peaks [33]. The abrasives scratch the sample surface is no longer along the single direction and are overlapped in the finishing zone instead, which reduces the unidirectional scratches and improves the surface quality.

The attention of this section is paid on clarifying the magnetic field distribution of MRF wheel and the available working bandwidth of NRVD. This is the basis for establishing the finishing force model and designing finishing experiments.
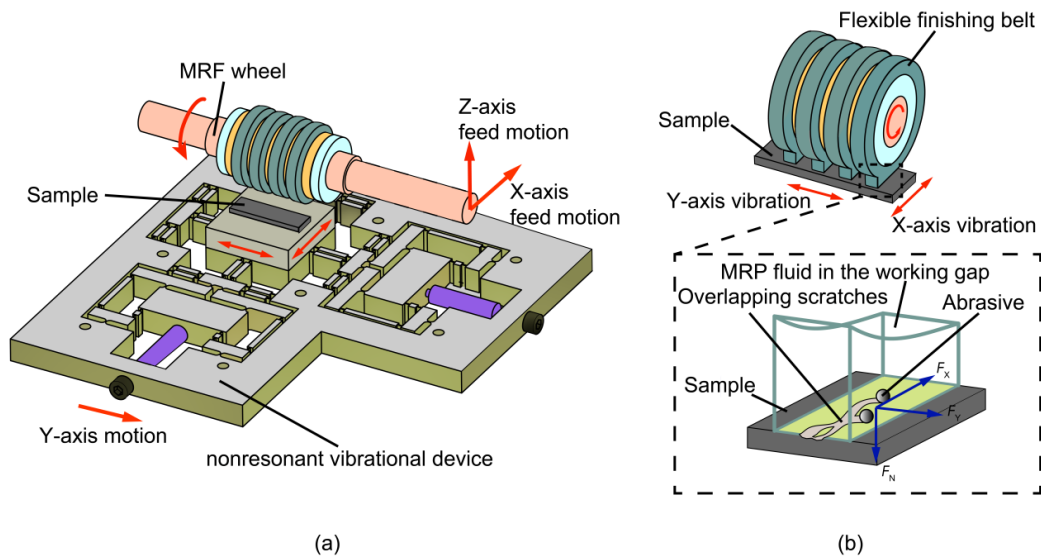

(a)   (b)

Fig.1. Schematic diagram of the WVMCF: (a) Key parts of the WVMCF. These parts include the MRF wheel with four flexible finishing belts and the nonresonant vibrational device that produces the 2D vibration. (b) Motion behavior of the abrasive particle under 2D vibration (2D vibration can be decomposed into Y-axis vibration and X-axis vibration). The partial enlarged detail of the finishing zone is in the black dashed outline. The blue arrows represent the finishing forces acting on the sample surface.

2.1 The new MRF wheel

Refers to the traditional MRF wheel, a single tubular magnet corresponding to a single flexible finishing belt [15]. One of the effective ways for improving the finishing efficiency is by increasing the number of finishing belts [37]. Based on this idea, the structure of the proposed MRF wheel is shown in Fig. 2a. Six identical tubular magnets made of neodymium-iron alloy with an outer diameter of 43 mm, an inner diameter of 25 mm, and a thickness is 4.5 mm (NdFeB, N38) are mounted on the aluminium shaft. Meanwhile, an aluminium loop (thickness of 5 mm) with the equal inner and outer diameters is installed between adjacent tubular magnets.

It is necessary to analyse the magnetic distribution generated by the wheel on the sample surface for determining the rheological parameters of an MRP fluid related to the magnetic flux density [38]. The AC/DC module of the COMSOL software was used to numerically study the magnetic distribution. The temperature was taken as the room temperature of T= 293.15 K, while the absolute pressure was taken as 1 atmosphere. A space around the magnet with the size of 60 mm × 60 mm × 60 mm was filled with air, while the relative permeability of the air was taken as 1. Both magnets and the space were meshed by standardized grid division. The minimum distance between the wheel and the sample was 0.5 mm.

The magnetic distribution is shown in Fig. 2b. The simulation results indicate that the magnetic flux density on the sample surface is mainly distributed in six regions denoted as *a*, *b*, *c*, *d*, *e*, and *f*, respectively. Due to the edge effect [39], the magnetic flux density significantly increases in ranges S_1 and S_2, which are located in regions *a* and *f*. In this case, the two outermost magnets are not used for processing to ensure the finishing effectiveness. The detailed step is that the MRF fluid is not sprayed on the surface of the two magnets during the machining process. Then, the flexible polishing ribbon cannot be produced by them. Since density magnitude and distribution in the rest areas are almost same, it is assumed that machining abilities and the finishing forces of four flexible finishing belts produced by MRF wheel are same [40]. Subsequent theoretical investigations are also based on this assumption.
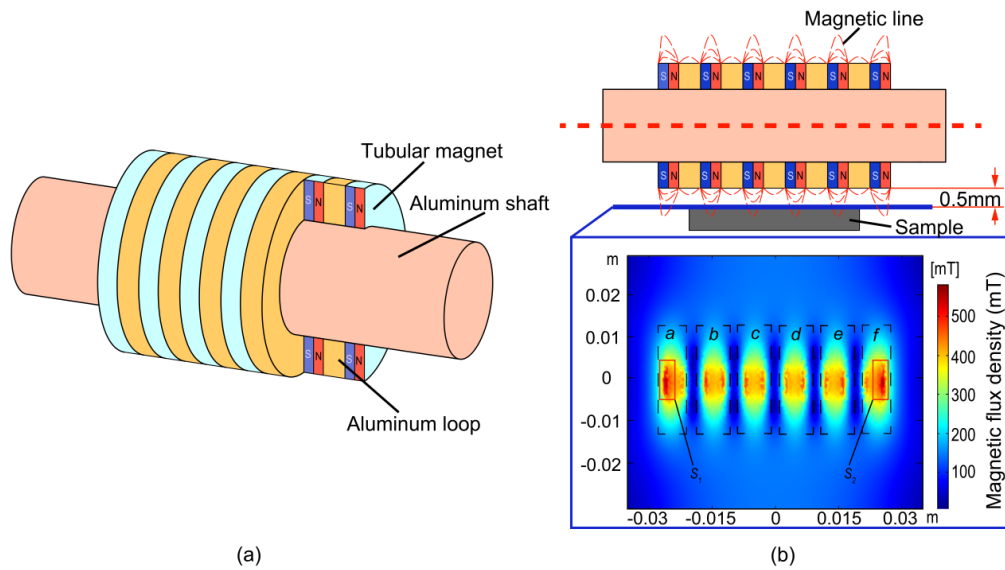

(a)   (b)

Fig. 2. Schematic diagram of the proposed MRF wheel: (a) structure of the MRF wheel. (b) simulation result of the magnetic flux density on the sample surface. The cloud image of the magnetic flux density distribution generated by the MRF wheel is in the blue solid outline. The magnetic density produced by each tubular magnet is in the black dashed outlines.
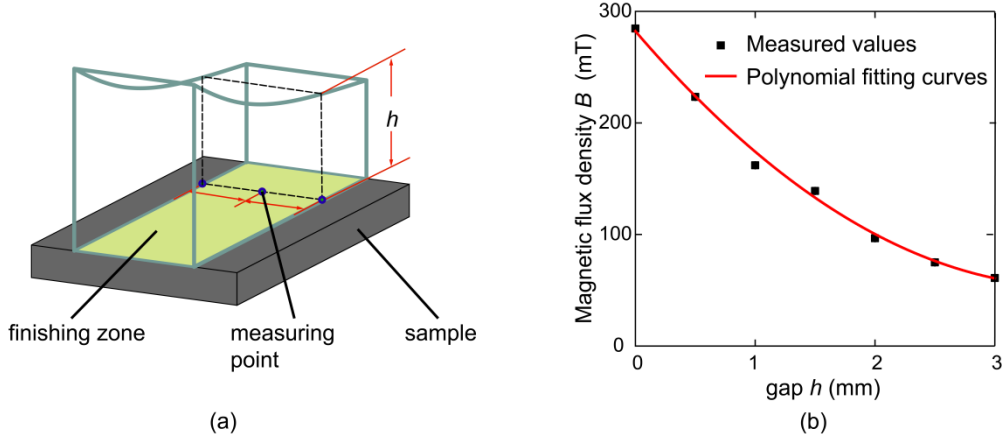

(a)   (b)

Fig. 3. The measured values and fitted curve of the magnetic flux density at different working gaps: (a) The measuring points at the working gap h. The position where the distance from the sample surface to the MRF wheel is h is the

intersection line between the black dashed outline and the finishing zone. The measuring points are located at the central position and left and right endpoints of the intersection line respectively. (b) The fitted results of the magnetic flux density. The red solid lines represent the fitted curve. The black points represent the measured values.

The magnetic flux density B in the finishing zone is simplified to a function related only to the working gap h. As shown in Fig. 3a, the density of three measuring points in the finishing zone at the gap h is measured using a Tesla meter. And the magnetic flux density is represented by the mean value of the measurements, are shown in Fig. 3b. The relationship between B and h can be described as follows (^{2}=0.98):

$$B(h)=282.238-125.133h+17.097h^2 \qquad (1)$$

2.2 The available working bandwidth of NRVD

A flexible mechanism is used to produce the targeted 2D vibration as its superior kinematic accuracy, frictionless , and controllable trajectory. However, the amplification parts in the mechanism designed to improve the displacement will weaken the structural stiffness and reduce the natural frequency of the device [41]. In this case, designing of these parts are crucial in the development of non-resonant devices.

Table1. The mechanical properties of the 7075AI

Components item (unit)	Value
Density ρ_1 (kg/m^3)	2810
Young's modulus E_1 (Gpa)	71.7
Poisson's ratio μ_1	0.33

To provide better displacement amplification effect, the differential lever is used as the flexible amplification mechanism [42]. The proposed NRVD has the same structure in both X and Y-axes. Thus, the amplification principle of the NRVD is introduced by considering the differential lever along the Y-axis for example. As shown in Fig. 4a, the NRVD provides 8 mounting holes that are used to fix during the actual machining process. A piezoelectric actuator (PZT) preloaded by the bolt applies an input force to the differential lever amplifier. The output displacement generated by the input force of the differential lever

amplifier is delivered by the guiding mechanisms to the sample located on the centre stage. Fig. 4b shows the amplification principle of the designed differential lever amplification mechanism. Under the action of the reversing lever, the input force makes the input point O_{in} and fulcrum O_f of differential lever to produce the opposite unidirectional displaces. Then, output displacement is generated at the output point Oout of the differential lever. Due to its lightweight and high yield strength under cyclic loading, aviation aluminium 7075AI was selected to make the NRVD material. Mechanical properties of the material are as Table 1 [43].

The output displacement and natural frequency of the NRVD were analyzed via ABAQUS software, as shown in Fig. 5. Fixed constraints for the finite element simulation of the device are shown in Fig. 5a. To simulate the fixed state of the actual situation, the inner wall of these mounting hole is set as the fixed constraint. The device simulations described below all used this fixed boundary. Theoretically, the same input force actuated at two input points will produce the same displacement due to the symmetry of the device. Therefore, only the maximum output displacement of the differential lever amplifier along the Y-axis is investigated. As shown in Fig. 5b, the output stage displacement is 66.14 μm with an input force of 1000 N. To avoid resonance damage, the working frequency of the device should not exceed its first natural frequency [16]. Thus, the natural frequencies of the NRVD were also analyzed. The simulation results of natural frequencies of the NRVD are shown in Fig. 5c, d, and e, respectively. The output point moves in a straight line along the X-axis and Y-axis at mode shape 1 and 2 and in the torsion around the Z-axis at mode shape 3, respectively. The first natural frequency of the device is 740.45 Hz.

Theoretically, the proposed NRVD can generate adjustable 2D vibration within an approximate working space of 66.14μm × 66.14μm. And, the maximum operating frequency is needed to ensure less than 740.45 Hz.
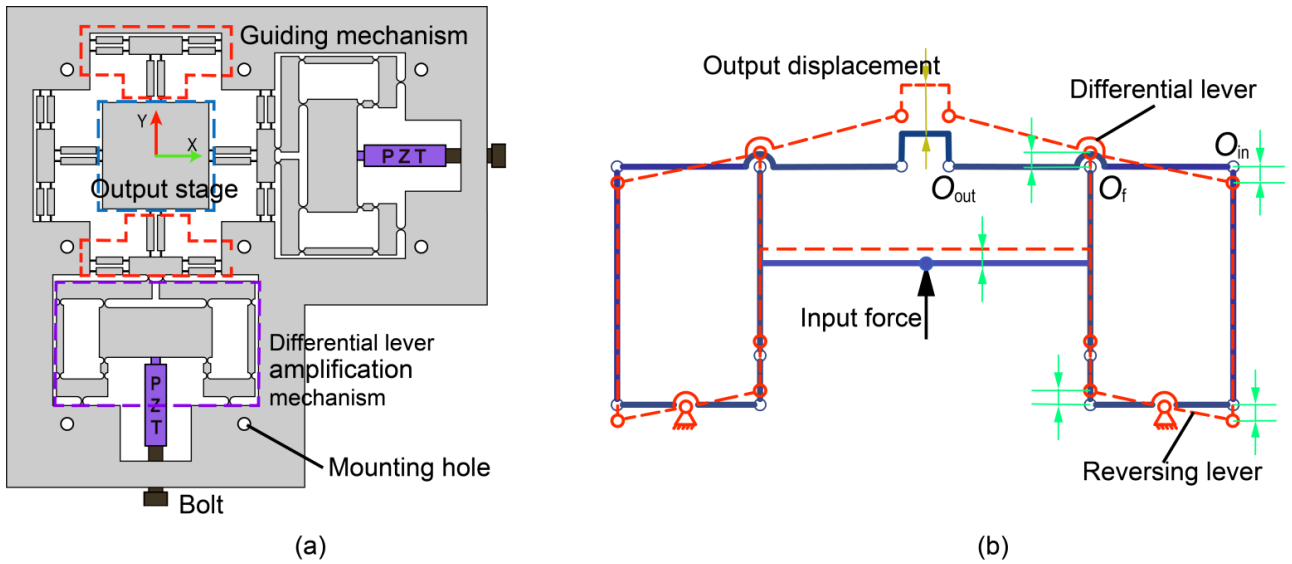
(a)

(b)

Fig. 4. Schematic diagram of the nonresonant vibrational device: (a) structure of the device. The red, blue and purple dashed outline represent the guiding mechanism, output stage and the differential lever amplification mechanism. (b) The amplification principle of the differential lever amplification mechanism. The connecting rod represents the rigid beam in the mechanism, and the motion pair represents the flexible hinge in the mechanism. The red dotted line and the blue solid line represent the state of the mechanism before and after applying the input force, respectively.

(a)

(b)

740.45Hz

748.69Hz

881.10Hz

(c)

(d)

(e)
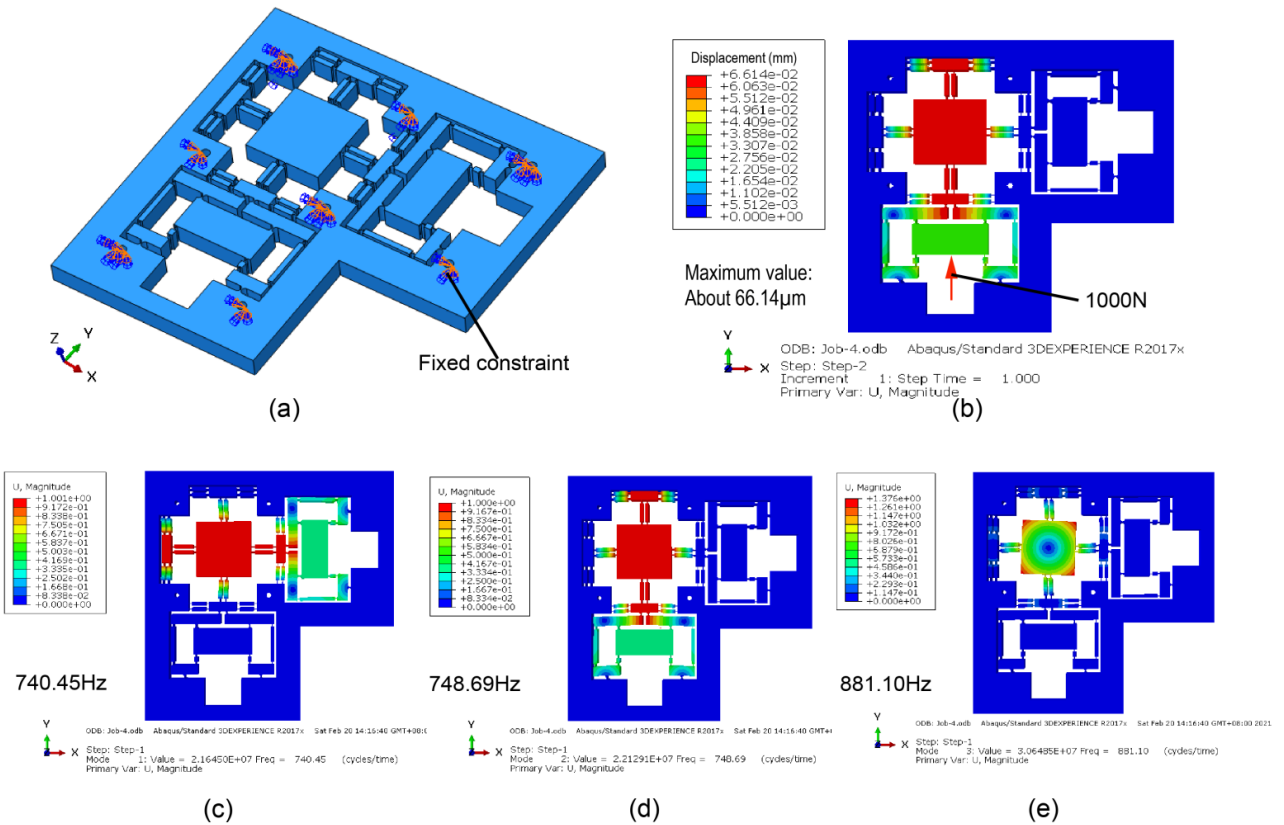
Fig. 5. Simulation results of the performance of the nonresonant vibrational device. (a) Fixed constraints for the finite element simulation of the device. (b) Simulation result of the Y-axes output displacement of the device. The red arrow represents the input force. (c) The first nature frequency and mode shape of the device, (d) The second nature frequency and mode shape of the device. (e) The third nature frequency and mode shape of the device.

3 Action mechanism of the XY planar vibration

In addition to the steady shear flow caused by the rotation of the MRF wheel, the micron XY planar vibration induced two-dimensional oscillatory shear flow of the MRP fluid in the finishing zone. The superposition of the two flow changes the fluid stress distribution. So the finishing forces are affected. In this section, a fluid flow model of the MRP fluid in this state was established. The finishing zone boundary, rheological, and viscoelastic properties of MRP fluid and other key parameters had been characterized before this.

3.1 Boundary quantifications of the finishing zone

The well-known method to determine the boundaries of processing areas is based on the plastic deformation produced by the contact between the flexible finishing belts and the sample [44]. And the geometric model of the contact area between the flexible finishing belt and the sample surface is shown in Fig. 6.

It is assumed that the finishing belts are incompressible and the wheel radius is R, the belt thickness is h_1, the minimum gap is h_0, and the immersion depth is D ($D = h_1 - h_0$), respectively. As shown in Fig. 6a, the profile of a single belt in the XOZ plane is a circle, which is concentric with the finishing wheel (the radius of the circle is $R + h_1$). Besides, the finishing belts are extruded, and the intersection point ranges from X_0 to X_1. The influence on the boundary can be neglected as the micro-order planar motion areas. And the effective length of the finishing zone, denoted as L, is the portion of the finishing belt in contact with the sample. In this case, the length L can be calculated as follows [45]:

$$\begin{cases} \int_{x_1}^{x_0} z\,dx = -\int_{x_0}^{0} z\,dx \\ z = R + h_1 - D - \sqrt{(R+h_1)^2 - x^2} \\ x_0^{\,2} = (R+h_1)^2 - (R+h_1-D)^2 \\ L = \left| x_1 \right| \end{cases} \tag{2}$$
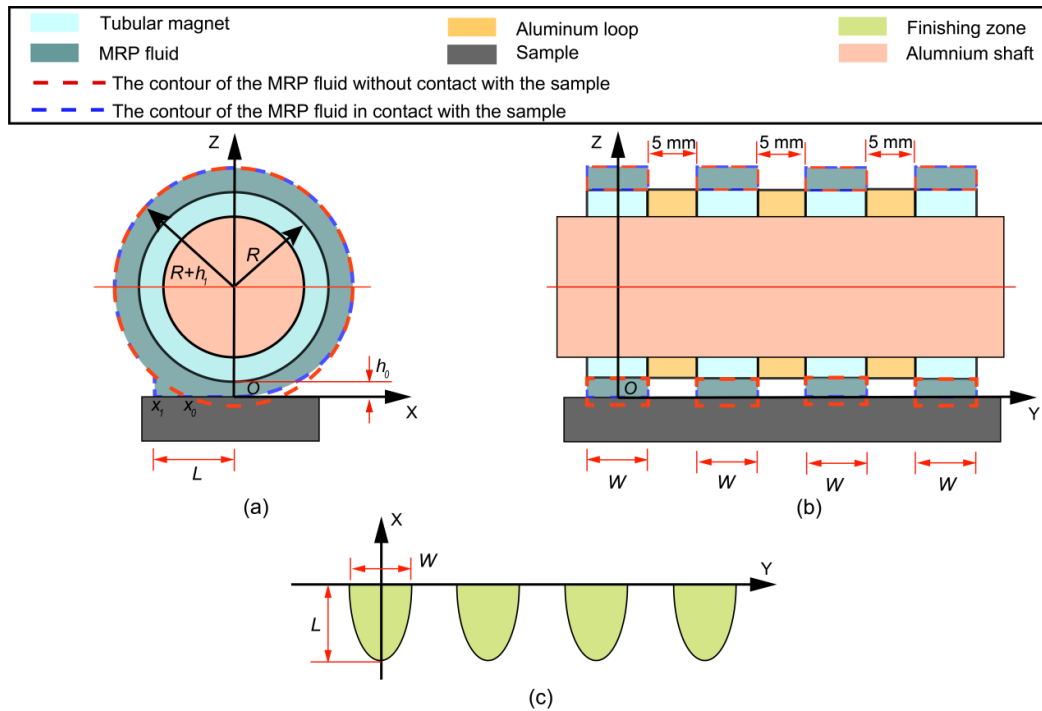

Fig. 6. Geometric model of the contact area (finishing zone) between the flexible finishing belt and the sample surface: (a) The length of the finishing zone. (b) The width of the finishing zone. (c) The shape of the finishing zone.

As shown in Fig. 6b, the effective width W of the finishing zone generated by a single flexible finishing belt is assumed as equal to the magnet thickness. The amplitude of the 2D vibration is on the micron scale. Therefore, the influence of it on the finishing zones boundaries is

ignored.The single zone that the flexible finishing belt intersects the sample surface is approximately viewed as "D" shaped. In the simplified finishing zones (Fig. 6c) proposed in this study, the zones boundaries are represented by four half ellipses. So, the finishing zones boundaries S are denoted as:

$$\frac{x^2}{L^2} + \frac{[y-(5+W)n]^2}{(W/2)^2} \leq 1$$

$$x \in [-L,0], y \in [-\frac{W}{2}+(W+5)n, \frac{W}{2}+(W+5)n]$$

(3)

3.2 Rheological properties of the MRP fluid

The magnetic particles of the water-based MRP fluid used in this study are carbonyl iron (CI) particles (average Particle size is 3 μm).Diamond Particles (Average size of 2.5 μm) were used as particles to remove surface roughness peaks because that they have great hardness than the samples (the material of the samples is silicon carbide). Glycerin is used as the wetting agent. Nano-silica is used as the thixotropic agent to improve the dispersion of fluids. Sodium hexametaponate is used as the preservative. Volume percentages of each component are shown in Table 2.

Table2. The volume percentages of each component of MRP fluid

Components item	Volume percentage
Water	ϕ_w =50%
CI particles	ϕ_C =40%
Abrasive	ϕ_a =5%
Nano-silica	ϕ_n =2%
Glycerol	ϕ_g =2%
Sodium hexametaphosphate	ϕ_s =1%

Contrary to the traditional method, the MRP fluid in the finishing zone flows under the coupling effect of steady shear and oscillating shear in WVMCF. Rheological properties of an MRP fluid under steady shear can be represented by the Bingham model [46]:

$$\tau = sign(\dot{\gamma})\tau_0 + \eta_1\dot{\gamma}$$

(4)

where τ is the shear stress of the MRP fluid, τ_0 is the shear yield stress under the external magnetic field, η_1 is the off-state viscosity, and $\dot{\gamma}$ is the shear rate. The shear yield stress τ_0 can be described as follows [47]:

$$\tau_0 = \left[1+\left(H/\alpha\phi_C^2 + \beta\phi_C + \chi\right)^{-B_{MRF}}\right]^{-1}$$
$$\times\left[4/5^{5/2} \cdot \xi(3) \cdot \phi_C \cdot \mu_0 \cdot M_s^2\right]$$

(5)

where ϕ_C is the volume fraction of CIPs in the MRP fluid, H is the magnetic field intensity ($H=B/\mu_0$), μ_0 is vacuum permeability (μ_0=4π × 10-7 T·m/A), M_s is the saturation magnetic field of magnetic particles (M_s =831.23 kA/m). Parameters α, β, χ, B_{MRF}, and $\xi(3)$ are constants (α =-1547.2 kA/m, β=844 kA/m, χ =-30.544 kA/m, B_{MRF} =-2.41, and $\xi(3)$ =1.202).

The MRP fluid under the normal condition is in the form of suspension. Its zero field viscosity η_1 can be described as [48]:

$$\eta_1 = \eta_0 \exp(2.5\phi/1-1.43\phi)$$

(6)

where η_0 is the viscosity of the base fluid ($\eta_0 = 2.89 \times 10^{-3} Pa \cdot s$) and ϕ is the volume fraction of all solid phases in the MRP fluid ($\phi = \phi_C + \phi_a + \phi_n$).

Viscoelastic characterization of the MRP fluid is a key scientific issue needed to be considered in the engineering applications [49]. In this paper, a simplified model is applied to characterize the viscoelastic behaviour of the MRP fluid under a complex flow field. As shown in Fig. 7a, the MRP fluid is characterized by complete CI particle strings and shows linear viscoelasticity when applied to a sufficiently small sinusoidal shear strain (i.e., linear viscoelastic range). In this case, its viscoelasticity can be characterized by the Kelvin-Voigt model in Fig. 7b.
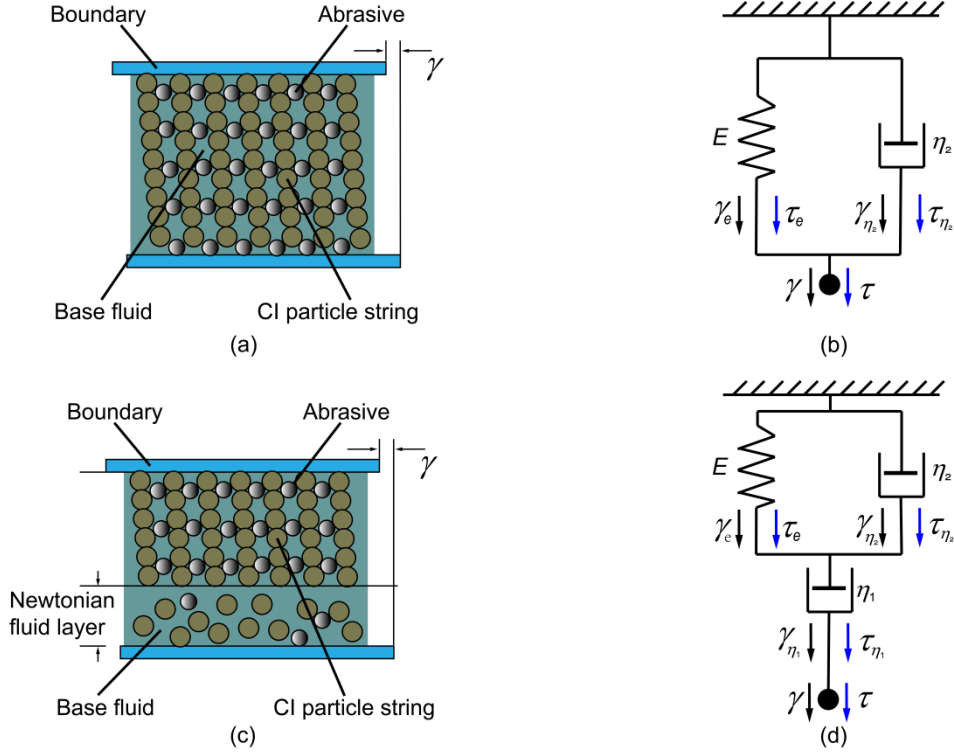
Fig. 7. Analog model used to represent the MRP fluid viscoelastic in the actual finishing process: (a) CI particle strings slightly tilted but intact strings at small sinusoidal shear strain. (b) Kelvin-Voigt model. (c) The MRP fluid yield and form a Newtonian fluid layer. (d) Three-parameter viscoelastic model.

The Kelvin-Voigt model consists of a spring unit and a sticky pot unit combined in a parallel mode. The spring unit is an ideal spring that satisfies Hook's law ($\tau_e = E \cdot \gamma_e$, where E is the ideal spring stiffness), and the sticker unit is an ideal Newtonian fluid ($\tau_\eta = \eta_2 \cdot \dot{\gamma}_\eta$, η_2 is the ideal Newtonian fluid viscosity) [50]. The stress τ_k and strain γ can be expressed as:

$$\tau_k = \tau_e + \tau_\eta \quad (7)$$

$$\gamma = \gamma_e = \gamma_\eta \quad (8)$$

By substituting $\tau_e = E\gamma_e$ and $\tau_\eta = \eta_2\dot{\gamma}_\eta$ into Eqs. (7) and (8):

$$\tau_k = E\gamma + \eta_2\dot{\gamma} \quad (9)$$

The response stress under oscillatory shear strain loading $\gamma = \gamma_0 \sin(2\pi ft)$ can be described as follows:

$$\tau_k = E\gamma_0 \sin(2\pi ft) + \eta_2 2\pi f \gamma_0 \cos(2\pi ft) \quad (10)$$

The feasibility of the model was verified in the previous study [51]. Parameters E and η_2 are mainly affected by magnetic field intensity and compositions of the MRP fluids,

respectively [52]. Moreover, they are insensitive to oscillatory shear strain [53]. But the CI particle strings that contact the sample surface will be destroyed. As shown in Fig. 7c, the MRP fluid will yield and form a Newtonian fluid layer [54]. To characterize the viscoelasticity of the MRP fluid in this state, the following assumptions are needed to be constructed:

(1) The rheological properties of MRP fluid are related to the structure of magnetic particle chains. In order to simplify the calculation, it is assumed that the rheological properties of MRP fluid in the machining gap are isotropic.

(2) The MRP fluid outside the Newtonian fluid layer still satisfies the Kelvin-Voigt model, and its spring stiffness and Newtonian fluid viscosity remain unchanged.

(3) The viscosity of the Newtonian fluid layer is the same as the zero-field viscosity of the MRP fluid.

Based on these assumptions and the Kelvin-Voigt model, a new viscoelastic model (three-parameter fluid model [55]) is formed by characterizing the viscoelastic properties of the MRP fluid during actual processing (Fig. 7d). Stress τ_t and strain γ of the proposed model can be expressed as:

$$\tau_t = \tau_{\eta_2} = \tau_e + \tau_{\eta_1} \tag{11}$$

$$\tau_t = \tau_{\eta_2} = \tau_e + \tau_{\eta_1} \tag{12}$$

Thus, the stress-strain expression of the model can be obtained [56]:

$$\eta_1\eta_2\ddot{\gamma} + \eta_2 E\dot{\gamma} = (\eta_1+\eta_2)\dot{\tau}_t + E\tau_t \tag{13}$$

$$\tau_t = \frac{E\eta_2^2(2\pi f)^2 + \left[(\eta_1+\eta_2)\eta_1\eta_2(2\pi f)^3 + E^2\eta_2(2\pi f)\right]i}{E^2 + (\eta_1+\eta_2)^2(2\pi f)^2}\gamma$$
$$= (G_1 + iG_2)\gamma = G^*\gamma \tag{14}$$

where G^* is the complex shear modulus, $\sqrt{i} = -1$. Parameters G_1 and G_2 are the real and imaginary parts of the complex shear modulus, respectively, can be represented as follows:

$$\begin{cases} G_1 = E\eta_2^2(2\pi f)^2 / \left[E^2 + (\eta_1+\eta_2)^2(2\pi f)^2\right] \\ G_2 = \dfrac{(\eta_1+\eta_2)\eta_1\eta_2(2\pi f)^3 + E^2\eta_2(2\pi f)}{E^2 + (\eta_1+\eta_2)^2(2\pi f)^2} \end{cases} \tag{15}$$

3.3 The normal force

To obtain the normal force F_N, the normal stress P_N in the finishing zone should be calculated first. A 2D vibration changes the shear flow boundary conditions of the MRP fluid. More specifically, the WVMCF is different from the conventional wheel-type MRF, which requires the establishment of a new fluid flow model based on the following assumptions:

(1) The gravity pressure of an MRP fluid are very small compared with the hydrodynamic pressure, which can be assumed as negligible.

(2) The fluid velocity at the fluid-solid boundary is equal to the fluid velocity at the solid boundary.

The total normal stress P_N is composed of hydrodynamic pressure P_d and magnetization pressure P_m generated by magnetic field. The magnetization pressure P_m is expressed as [57]:

$$P_m = \phi\mu_0\mu_f \frac{3(\mu_p-\mu_f)}{2(\mu_p+2\mu_f)}\left(\frac{B/\mu_0}{1+3\mu_0\mu_f\dfrac{\mu_p-\mu_f}{\mu_p+2\mu_f}}\right)^2 \tag{16}$$

Where, μ_f is the magneto conductivity of the water($4\pi\times10^{-7}H/m$), μ_p is the magneto conductivity of magnetic particle($2\times10^{-3}H/m$); ϕ_c is the volume percentage of CI particles，and B is the magnetic flux densities in the finishing zone.

The shear flow of the MRP fluid is shown in Fig. 8. The shear flow boundary condition of the MRP fluid in the ZX-plane is shown in Fig. 8a. The minimum gap h_0 has kept constant. Thus, the value of the working gap h can be simplified as:
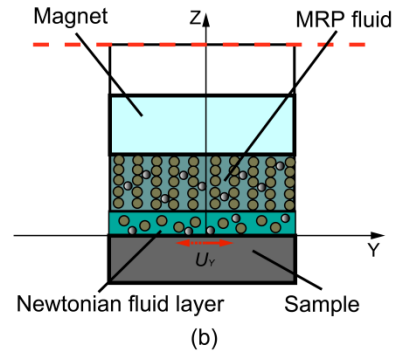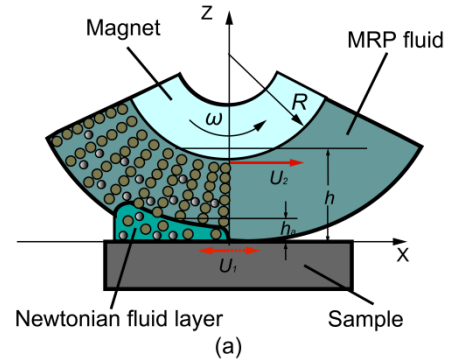
$$h = h_0 + x^2/2R \tag{17}$$

Fig. 8. Flow model of MRP fluid under the combined action of rotation of polishing wheel and vibration of sample: (a) Shear flow boundary conditions of MRP fluid in the ZX-plane, and (b) Shear flow boundary conditions of MRP fluid in the ZY-plane. The red arrows represent velocity boundary conditions for fluid flow.

However, the corrected working gap depends on the previously mentioned thickness of the Newtonian fluid layer, which is related to the shear rate [54]. And the additional vibration will change the thickness by affecting the shear rate. In this case, working gap requires correction. In this paper, a gap correction coefficient $k = k(f, A)$ is

introduced to facilitate calculation. Thus, the corrected minimum gap after correction h_{m0} is:

$$h = h_0 + x^2/2R \tag{18}$$

By combining Eqs. (17) and (18), the equivalent working gap h_a can be expressed as follows:

$$h_a = h_{m0} + x^2/2R \tag{19}$$

The sample equipped with an amplitude of A_1 and a frequency of f_1 moves harmonically along the X-axis. In this case, the movement velocity U_1 of the sample surface is:

$$U_1 = A_1 2\pi f_1 \cos(2\pi f_1 t) \tag{20}$$

The MRF wheel rotates at an angular velocity ω. Thus, the linear velocity near the core U_2 is:

$$U_2 = \omega R \tag{21}$$

The Reynolds equation of the fluid flow in the convergence gap is expressed as [57]:

$$dP_d/dx = 6\eta_1 U(\frac{h_a - h^*}{h_a^3}) \tag{22}$$

where $U = U_1 + U_2$, and h^* is the thickness corresponding to the maximum pressure.

To obtain h^*, the following substitution equation is used [58]:

$$\tan\theta = x / \sqrt{2Rh_{m0}} \tag{23}$$

where θ is the substitution angle, which is the substitution variable introduced for the operation.

After derivation (see Appendix 1 for the process), the h^* is obtained:

$$h^* = 4/3\, h_{m0} \tag{24}$$

By combining Eq. (21) and (23), the pressure gradient dP_d/dx can be obtained as:

$$dP_d/dx = 6\eta_1 U(\frac{h_a - 4/3 h_{m0}}{h_a^3}) \tag{25}$$

After deduction (see Appendix A), the P_d is obtained:

$$P_d = \frac{-2\eta_1 \left[\omega R + A_1 2\pi f_1 \cos(2\pi f_1 t) \right] x}{(k h_0 + \frac{x^2}{2R})^2} \tag{26}$$

The total normal stress P_N is then equal to:

$$P_N = P_d + P_m \tag{27}$$

The normal force F_N is obtained by integrating the total normal stress P_N in the boundary of the finishing zone S:

$$F_N = \iint_S P_N dS \tag{28}$$

3.4 The tangential force

To obtain the tangential force, total shear stress includes shear stress τ_X and τ_Y along X-axis and Y-axis, respectively, in finishing zone boundaries S should be calculated. The X-axis shear stress τ_X consists of steady shear stress τ_1 and oscillatory shear stress τ_2:

$$\tau_X = \tau_1 + \tau_2 \tag{29}$$

According to the lubrication theory, the distribution of the steady shear stress τ_1 is related to the pressure gradient dP_d/dx. Thus, fluid shear stress distribution $\tau_1(x, z)$ can be expressed as [59]:

$$\tau_1(x, z) = \frac{dp_d}{dx}(z - \frac{h_a}{2}) - \frac{\eta_1 U}{h_a} - \tau_0 \tag{30}$$

And the steady shear stress on the machined sample surface is equal to:

$$\tau_1(x, z)\big|_{z=0} = -\frac{h_a}{2}\frac{dp_d}{dx} - \frac{\eta_1 U}{h_a} - \tau_0 \tag{31}$$

By substituting Eqs. (18), (19), (20), (21), and (25) into Eq. (31), the steady shear stress τ_1 is calculated as:

$$\tau_1 = -\frac{8\eta_1 \omega R^2 x^2}{(2Rk h_0 + x^2)^2} - \tau_0 \tag{32}$$

The X-axis oscillatory shear strain γ_X is equal to:

$$\gamma_X = \frac{A_1}{h}\sin(2\pi f_1 t) \tag{33}$$

Then, the response stress τ_2 caused by vibration along the X direction is expressed as follow [60]:

$$\tau_2 = \frac{A_1\sqrt{G_a'^2 + G_a''^2}\sin(2\pi f t + \delta)}{h_0 + \frac{x^2}{2R}} \tag{34}$$

where $\delta = \arctan(G_a''/G_a')$. The X-axis tangential force F_X is obtained by integrating the total shear stress τ_X in the boundary of the finishing zone S:

$$F_X = \iint_S \tau_X dx dy \tag{35}$$

The flow caused by the vibration along y direction is shown in Fig. 8b. The Y-axis and the Z-axis is located and perpendicular to the sample, respectively. And this sample moves in sinusoidal motion with the amplitude of A_2 and the frequency of f_2 along the Y-axis begin with the origin of O. Thus, the Y-axis oscillatory shear strain γ_Y is:

$$\gamma_Y = \frac{A_2}{h}\sin(2\pi f_2 t) \tag{36}$$

The MRP fluid is only affected by the Y-axis vibration on the ZOY plane as the velocity of the MRF wheel along the Y-axis is 0. In this case, the Y-axis shear stress τ_Y only includes oscillatory shear stress and it can be expressed as:

$$\tau_Y = \frac{A_2\sqrt{G_a'^2 + G_a''^2}\sin(2\pi f_2 t + \delta)}{h_0 + \dfrac{x^2}{2R}} \tag{37}$$

So the Y-axes tangential force F_Y is obtained by integrating the shear stress τ_Y in the boundary of the finishing zone S:

$$F_Y = \iint\limits_S \tau_Y dxdy \tag{38}$$

According to the above model, the quantitative method of finishing forces is given. To facilitate analysis, the mean values of the forces are calculated by integrating the time period of vibration cycle. Thus, theoretical values of normal force $\overline{F_N}$, X-axes tangential force $\overline{F_X}$, and, Y-axes tangential force $\overline{F_Y}$ are respectively equal to:

$$\begin{cases} \overline{F_N} = \dfrac{1}{T}\int_0^T |F_N| dt \\[2mm] \overline{F_X} = \dfrac{1}{T}\int_0^T |F_X| dt \\[2mm] \overline{F_Y} = \dfrac{1}{T}\int_0^T |F_Y| dt \end{cases} \tag{39}$$

where T is the vibration period of and $T = 1/f$ ($f = f_1 = f_2$).

4 Device test and processing experiments

As can be seen from the finishing force model in the previous section, vibration parameters such as amplitude and frequency can make significant contribution to the processing of the WVMCF. However, the actual operating areas of NRVD should be determined before designing processing experiment. Thus, the required parameters of the NRVD are marked by the on-line testing experiments. Finally, the experimental setup and parameters are given in this section.

4.1 Performance test of the NRVD

As shown in Fig. 9, the test system was set on a vibration isolation platform. A controller (Power PMAC, E-500, PI Inc.) generated the commanded position signal connected to the power amplifier. Then amplified signal from the power amplifier drove the piezoelectric actuator (PZT) to generate the input force on the NRVD to produce the desired output displacement. Capacitance sensors (2805, MicroSense Inc.) and position measurement system (DE 5300-013, MicroSense Inc.) collected the output displacement and then the signal was sent back to the controller. Commanded position signal and the actual position signal were processed and drawn by a personal computer (PC).
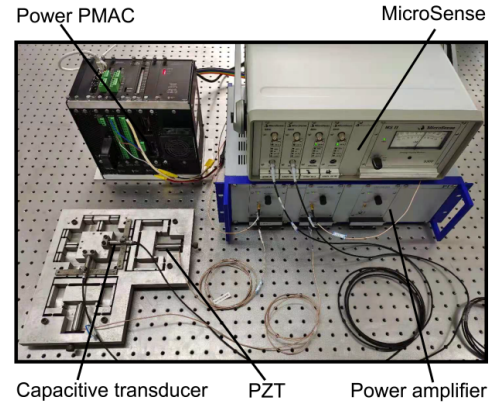

Fig. 9. The performance test system of the nonresonant vibrational device.

As shown in Fig. 10, actual maximum effective displacements of the device along the X and Y-axes were tested, respectively, through applying the step position signal to the PZTs. The results indicate that the actual X-axis position agrees well with the command position signal and the maximum effective displacement of 60 μm is achieved. Meanwhile, the actual Y-axis position also shows a good agreement with the command position signal and the maximum effective displacement of 50 μm is reached. It is obvious to catch the certain difference caused by manufacturing errors exists between maximum effective displacements along X and Y-axes. But, these values can still meet the design goals and experimental requirements.
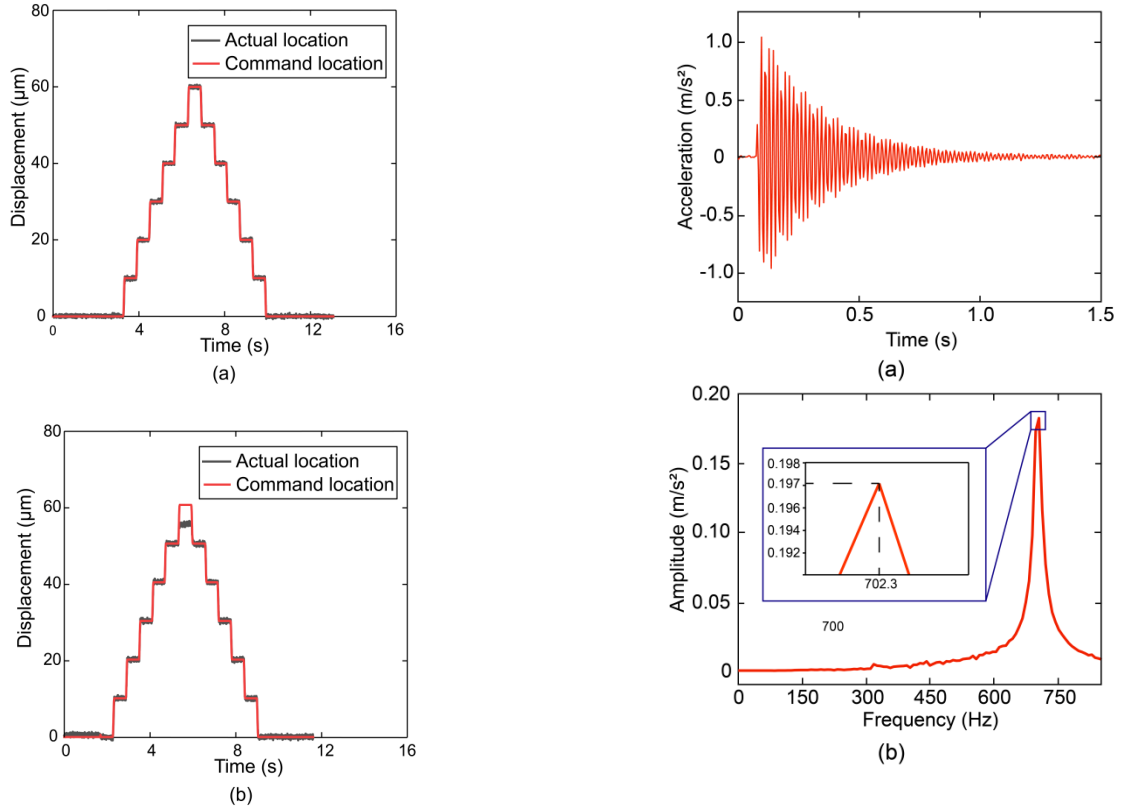
(a)

(b)

Fig. 10. Effective displacements test results of the nonresonant vibrational device. The red solid lines represent the instruction signal of the displacements generated by the controller, and the incremental step is set to 10 μm. The black solid lines represent the actual tracking signals of displacements generated by nonresonant vibrational device received by the displacement sensor. (a) X-axis displacement, and (b) Y-axis displacement.

In this next step, the natural frequency of the device was tested based on using the impact hammer to knock excited point and collected the related response data. The acceleration response signal (shown in Fig. 11a) was obtained by the second-order differentiation of the gained displacement data. The self-power spectrum of the device was obtained by conducting a Fourier transform on the acceleration response signal. As shown in Fig. 11b, the first-order natural frequency is approximately equal to 702.3 Hz. Deviations between the FEM and experimental results may be due to the assembly errors. Nevertheless, the natural frequency still operate well as the device can work below this frequency during the VWMRF process. In summary, the NRVD has an ideal actual vibration performance and can play the fundamental role in the finishing experiments. The selected vibration parameters are referred in the next section.

(a)

(b)

Fig.11. Dynamic response test results of the nonresonant vibrational device. (a) The acceleration signal in time domain. It is obtained by the second derivative of the displacement quotation marks measured by the displacement sensor, and (b) The first natural frequency in the frequency domain. It obtained by Fourier transform of the acceleration signal. The partial enlarged detail of the frequency peak point is in the blue solid outline.

4.2 Finishing experiments

As shown in Fig.12, the MRF wheel was connected by a coupling to an electric motor that produced rotary motion about its rotation axes. The X-axis position of the wheel was adjusted by servomechanism 1. And the Y-axis position of the NRVD was adjusted by manual. Furthermore, the Z-axis position was adjusted by servomechanisms 2 and 3 at the same time to allow the control of the working gap between the sample and tool. The sample was fixed on the NRVD by a 3D printing fixture. As a typical hardness brittle material, the pressureless sintered silicon carbide ceramic with the size of 40 mm × 10 mm × 5 mm was selected as the sample. And these samples were pre-treated by a grinding machine before the experiments. During the experiments, the power amplifier (PI, E-500) was used to magnify the control signals generated by the signal generator and sent them to the two PZTs. After correct alignment of the finishing wheel, the dynamometer (Kistler, 9257B) under the NRVD along the Z-axis measured the finishing forces accurately during the WVMCF. And then the force signals amplified by a charge amplifier were transmitted to a data acquisition card and

drawn by another PC. In this study, it was controled by controlling the volume of spraying MRP fluid that the thickness of a belt . The measured thickness of the ribbon is about 0.6mm when spraying 1ml MRP fluid onto an annular magnet surface of the polishing wheel and applying evenly. Therefore, the spraying amount of MRP fluid on each annular magnet surface was controlled to be 1ml in all finishing experiments. The MRP fluid was substituted every 10 minutes to reduce the effect of the fluid properties changes. After the experiments, the surface roughness of the sample was measured by a white light interferometer (Zygo, NewView 8000). Four randomly selected points in the finishing zone were measured, and the surface roughness Sa and Sz average values of these points was given as below. The parameters of each finishing experiment are summarized in Table 3. The machining effect of the MRF without introducing vibration was investigated by conducting Experiment 1. In order to make comparision, the influence of changing operating frequency was shown in Experiment 2. Finally, the effects of applying different amplitude values were considered in Experiment 3. These experiments were repeated three times for each group.

Table3. Finishing Parameter setting

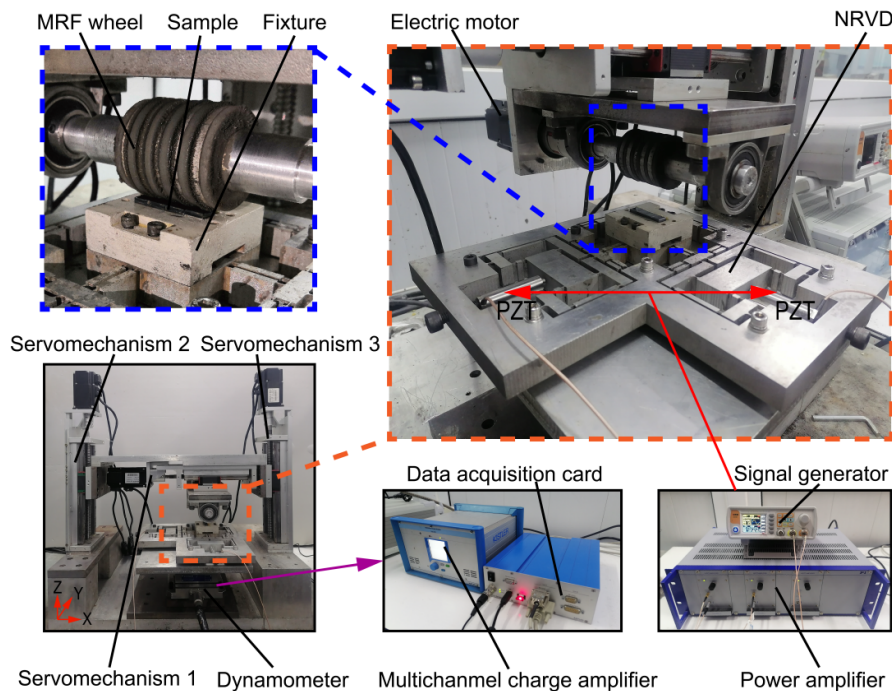| Finishing Parameter （units）	Experiment 1	Experiment 2	Experiment 3
Initial average surface roughness Sa (nm)	~70	~70	~70
MRP fluid ribbon thickness h_1 (mm)	0.6	0.6	0.6
Minimum finishing gap h_0 (mm)	0.5	0.5	0.5
MRF wheel diameter R (mm)	21.5	21.5	21.5
MRF wheel speed ω (rpm)	100	100	100
Amplitudes $A = A_1 = A_2$ (μm)	0	35	25,35,45
Frequencies $f = f_1 = f_2$ (Hz)	0	150,250,350	300
Finishing time t (min)	30	30	30

Fig.12. Finishing experimental setup. The partial enlarged detail of the non-resonant vibration generator, MRF wheel, and sample and fixture are in the orange dashed outline. The partial enlarged detail of the MRF wheel in contact with the sample is in the blue dashed outline. The purple arrow represents the force signal output by the dynamometer, and the red arrow represents the control signal generated by the signal generator.

5.Results and discussions

5.1 Determination of model coefficients

In this section, the coefficients in the model are determined by the results of dynamometer measurement. Table 4 shows the experimental values (mean ± standard deviation) of tangential and normal forces based on the measured data at different amplitudes and frequencies.

Based on mean values of the forces, the gap correction coefficient k, spring stiffnes E, and ideal Newtonian fluid viscosity η_2 in the model are fitted, and the fitting results are shown in the table.

Table4. Finishing forces and fitting coefficients

parameters		measured finishing forces			fitting results
A (μm)	f (Hz)	F_X (N)	F_Y (N)	F_N (N)	
0	0	1.901±0.084	0.011±0.005	2.690±0.200	
35	150	3.202±0.067	0.947±0.051	3.132±0.042	
35	250	3.358±0.472	1.550±0.127	3.576±0.531	$k(f,A)$=0.008 $-6.2553×10^{-9}A^2f$ (R^2=0.94)
35	350	4.576±0.436	3.299±0.307	3.870±0.432	
25	300	3.489±0.534	1.406±0.175	3.378±0.170	E=2×10^6 Pa
35	300	3.992±0.379	1.663±0.120	3.872±0.398	η_2 =483 $Pa \cdot s$
45	300	5.416±0.404	1.942±0.074	4.831±0.059	

5.2 The surface quality without vibration

The related experimental parameters are shown in Experiment 1 in Table 3. Typical surface morphologies of the samples before and after processing are shown in Fig. 13, respectively. As shown in Fig. 13a, the initial sample surface has a large number of randomly distributed asperities and valleys, which are the results of pre-treated processes. The surface morphology of the sample after finishing without vibration is shown in Fig. 13b. After 30 minutes of finishing, the Sz value of the sample surface is reduced from 5.995 μm to 3.451 μm. However, the unidirectional scratches produced by abrasive particles on the sample surface and it absolutely deteriorates the surface accuracy (the Sa value increases from 69 nm to 123 nm).
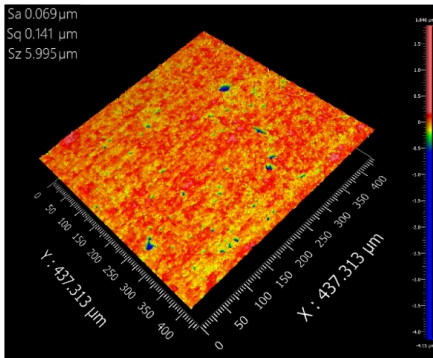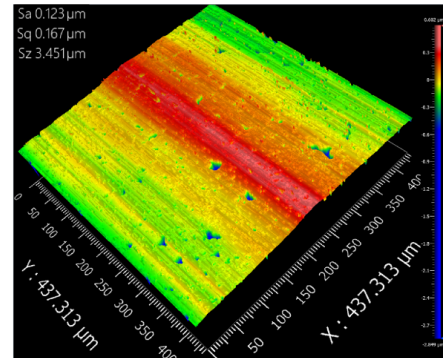

(b)

Fig.13. The sample surface roughness and morphology before and after finishing without vibration: (a) The initial surface after the pretreatment. (b) The sample surface roughness and morphology of the surface after finishing using the MRF wheel alone.

To better understand the influence mechanism of applying planar vibration on the sample surface, the surface micro-topographies after MRF were measured by a scanning electron microscope (SEM). As shown in Fig.14a, it can be observed that numerous regular linear scratches distributed along the same direction after finishing without introducing vibration. The reason to this unwanted phenomenon is the finishing forces acting on the abrasive particles which engaged in the targeted sample as there is no tangential forces are present in the Y-axis. And the abrasive particles move only under the action of the X-axis tangential force.

(a)

These scratches cannot be removed because of the tangential force performed at the same direction with the scratches. Eventually, as shown in Fig.14b, they accumulate after machining circles on the surface of the sample and lead to generate unidirectional scratches. In addition to scratches, there are some pits that can be seen on the surface of the sample. These pits in the SEM image maybe original pores hidden under the surface during the preparation of these non-pressure sintered silicon carbide samples. When the surface material is removed, the pores are exposed to form pits. Zhang et al. [61] also found that there were pits on the workpiece surface when they used a bonnet tool to polish pressureless sintered silicon carbide. They confirmed these pits were original micro holes hidden under the surface of the workpiece, rather than the damage caused by the processing method.
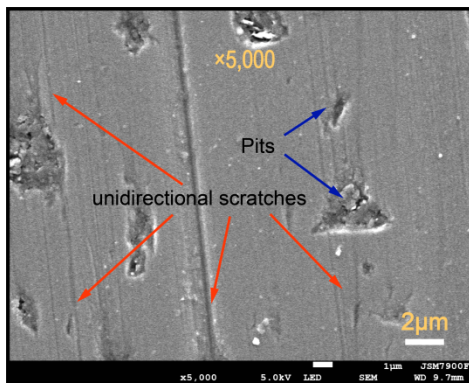
(a)
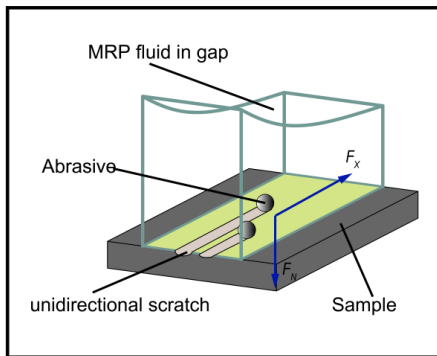
(b)

Fig.14. Effect of the finishing forces without vibration on motion behavior: (a) The SEM images of the sample surfaces without vibration. The magnification is 5000 times. The positions marked by the red arrows are unidirectional scratches. (b) The process of removing material from sample surface by abrasive particles without vibration. The blue arrows represent the finishing forces, and the direction of the arrow is the direction of the force.

5.3 Effect of the vibration frequency

In this section, the experiment related to the effect of changing frequency is conducted and the related experimental parameters are demonstrated in Experiment 2 in Table 3. Typical surface morphologies at different vibration frequencies are shown in Fig.15. As shown in Fig. 15a, the sample surface still has obvious unidirectional scratches at the frequency of 150 Hz. However, surface roughness Sa value is significantly lower compared to the sample without introducing vibration (from 123 nm to 79 nm). As shown in Fig. 15b, it can be also observed that the unidirectional scratches are present on the sample surface at a frequency of 250 Hz. But they are sparse and shallow. Surface roughness Sa values of the sample further decrease (decreased to 46 nm). As shown in Fig. 15c, the unidirectional scratches of the sample surface are not obvious at the frequency of 350 Hz. The Sa values of the sample surface compared with the finishing without vibration decreased to 17 nm. Moreover, the surface tends to be uniform. These results indicate that surface quality increases with vibration frequency.
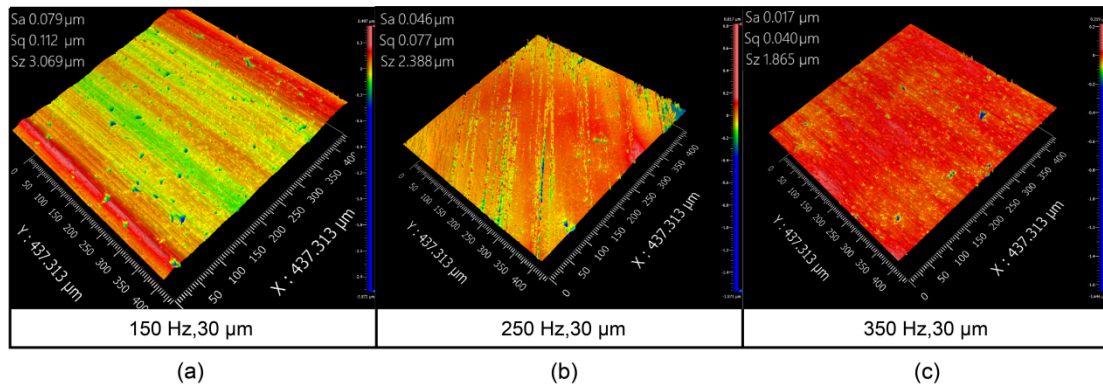
Fig.15. The sample surface roughness and morphology after finishing with different vibration frequencies: (a) at 150 Hz, (b) at 250 Hz, and (c) at 350 Hz.

The reason why the surface roughness decreases with increasing frequency is the influence of vibration frequency on finishing forces. The finishing forces at different vibration frequencies are shown in Fig. 16. The normal force and X-axis tangential force are significantly increased compared with the condition without vibration. An additional Y-axis tangential force is generated, and it increases with vibration frequency. The theoretical values of normal force and X-axis tangential force agree well with the experimental, which verifies the validity of the model. Only under the processing condition with the frequency of 350 Hz, the error between the theoretical and experimental values of the X-axis tangential force is slightly larger. The theoretical values of the Y-axis tangential force are slightly smaller than the experimental. The reason for this phenomenon may be that the magnetic line is directional. In this paper, magnetic lines parallel to the Y-axis cause magnetic particles to form chain columnar structures along the Y-axis. This results in the difference in the chain structure of the MRP fluid in the direction of X and Y-axes. It is assumed that the rheological properties of the MRP fluid are isotropic in the process of polishing force modeling. It is ignored that the difference of rheological properties in different directions, which eventually leads to this result.
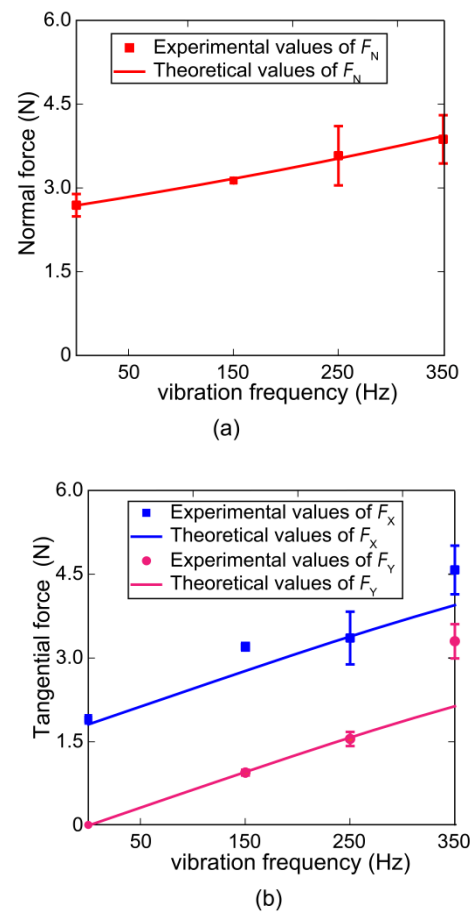

Fig.16. Experimental and theoretical values of normal force, X and Y-axis tangential forces under different vibration frequencies: (a) Normal force, and (b) tangential force. The theoretical values are expressed as continuous solid lines and the forces in the range f=0 Hz to f=350 Hz are calculated. Experimental values are represented by error bars. The forces at f=0 Hz, f=150 Hz, f=250 Hz, and f=350 Hz were measured and the mean and standard deviation were calculated. The normal force is represented by the red solid

line and error bar, the X-axis tangential force is represented by the blue, and the Y-axis tangential force is represented by the pink.

It can be seen from Eq. 26 that increasing vibration frequency can increase the shear rate and reduce the thickness of the Newtonian fluid layer, which means that the fluid dynamic pressure in the finishing zone increases. It increases the normal force exerted by an abrasive particle on the sample surface. And, the depth of the abrasive particle pressed into the sample surface increases. Eq. 15 shows that the composite shear modulus of the MRP fluid increases with the frequency. As can be seen from Eqs. 29 and 37, the increased composite shear modulus will increase the total shear stress. It not only increases the tangential force exerted by the abrasive particles on the sample surface, but also forces the abrasive particles to constantly change the direction of motion due to the extra Y-axis oscillation shear stress. The abrasive particles pressed into the sample surface no longer move in a single direction, which effectively reduces the production of linear scratches. In conclusion, normal and tangential forces increase with the vibration frequency. The ability of abrasive to remove surface roughness peaks is enhanced. The Y-axis tangential force increases with the vibration frequency, which makes the abrasive more and more deviate from the straight path. These cause the surface roughness to decrease with increasing frequency. The SEM image of the sample surfaces after finishing at f=350 Hz and A=35 μm is as shown in Fig.17. Although pits and few scratches exist on the surface, 2D vibration effectively inhibits the generation of linear scratches. The surface quality is effectively improved.
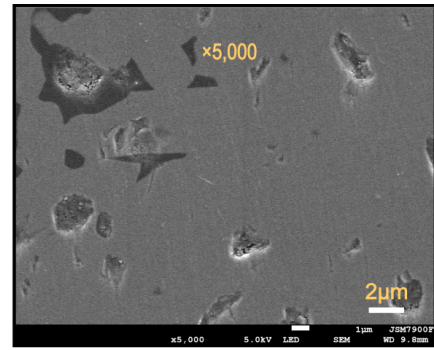

Fig.17. The SEM image of the sample surfaces after finishing at f=350 Hz and A=35 μm. The magnification is 5000 times.

5.4 Effect of the amplitude

In this section, the experiment related to the effect of changing amplitude is conducted and the related experimental parameters are demonstrated in Experiment 3 in Table 3. Typical surface morphologies at different amplitudes as below. As shown in Fig. 18a, the sample surface has sparse and shallow unidirectional scratches at the amplitude of 25μm. However, surface roughness Sa value is significantly lower compared to the sample without introducing vibration (decreased to 79 nm). As shown in Fig. 18b, there are seldom unidirectional scratches on the sample surface at the amplitude of 35μm. Surface roughness Sa values of the sample further decrease (decreased to 32 nm). As shown in Fig. 18c, the surface tends to be uniform at the amplitude of 45μm. The Sa values of the sample surface compared with the finishing without vibration decreased to 20 nm. These results indicate that surface quality increases with amplitude.
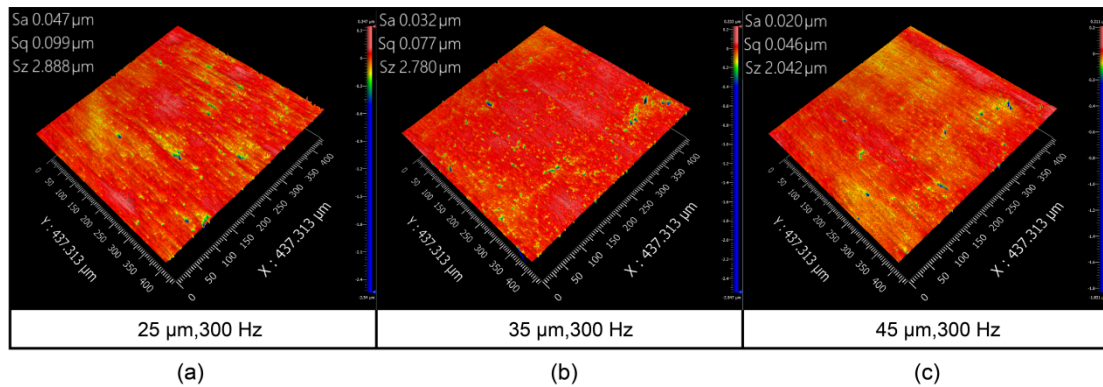

Fig.18. The sample surface roughness and morphology after finishing at different amplitudes: (a) at A=25 μm, (b) at A=35 μm, and (c) at A=25 μm.

Another key factor for improving the surface quality via the 2D vibration is the influence of amplitude on finishing forces. Finishing forces at different amplitudes are shown in Fig. 19. Both the tangential force and the normal force are

positively correlated with amplitude. It is similar to the effect of increasing the frequency. But, it has more obvious effect on normal force compared with frequency. Similar to the situation in Fig.16, the theoretical values of normal force and X-axis tangential force are in agreement with the actual values, which verifies the validity of the model. But, the theoretical values of the Y-axis tangential force are slightly smaller than the experiment. The reason for this phenomenon may also be the different chain structures in the X and Y directions. The rheological properties of the MRP fluid vary in different directions. It eventually leads to deviation.

It can be seen from Eq. 26 that increasing amplitude can also increase the fluid dynamic pressure by increasing the shear rate and reducing the thickness of the Newton fluid layer. It can be seen from the fitting gap correction coefficient k in Table 4 that the action mechanism of the amplitude is slightly different from that of frequency, which has a greater influence on the equivalent thickness of the Newtonian fluid layer (quadratic relation). Eq. 15 may not shows the effect of amplitude on the compound shear modulus of MRP fluid. However, it can be seen from Eqs. 29 and 37 that increasing the amplitude can increase the total shear stress by increasing the oscillatory shear strain. As the amplitude increases, the normal and tangential forces also increase. The ability of abrasive to remove surface roughness peaks is enhanced. The Y-axis tangential force increases with the amplitude, which makes the abrasive more and more deviate from the straight path. These cause the surface roughness to decrease as the amplitude increases.
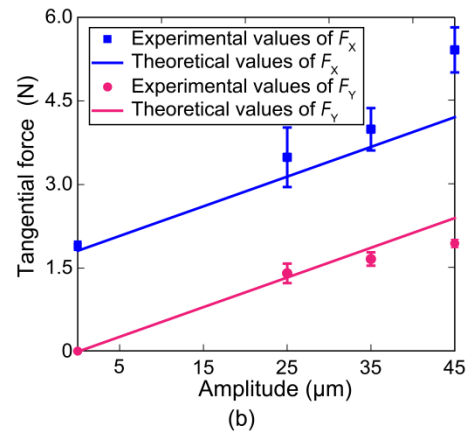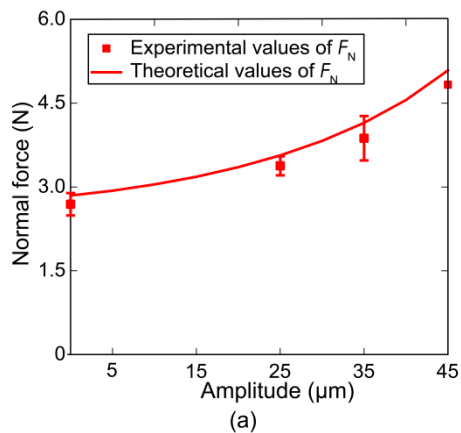

(a)

(b)

Fig.19. Experimental and theoretical values of normal force, X and Y-axis tangential forces under different amplitudes: (a) Normal force and (b) tangential force. The theoretical values are expressed as continuous solid lines and the forces in the range 0 to 45 microns are calculated. Experimental values are represented by error bars. The forces at A=0 μm, A=25 μm, A=35 μm, and A=45 were measured and the mean and standard deviation were calculated. The normal force is represented by the red solid line and error bar, the X-axis tangential force is represented by the blue, and the Y-axis tangential force is represented by the pink.

6 CONCLUSION

In this paper, a wheel-type vibration-magnetorheological compound finishing (WVMCF) was proposed to extend the current finishing methods. The influence mechanism of the 2D vibration was demonstrated by analyzing the finishing forces. A series of processing experiments were conducted to evaluate the performance and feasibility of the developed method. Lastly, the relationship between the vibration parameters and the measured finishing forces, and surface quality was quantitatively and qualitatively analysis. The conclusions are as follows:

(1) Based on the theoretical analysis and experimental phenomenon, it is found that the tangential force in a single direction produces directional scratches in MRF based on a wheel tool. The scratches worsened the surface accuracy compared to the initial surface of the sample. The surface roughness Sa value increases from 69 nm to 123 nm.

(2) 2D vibration significantly improves the normal and tangential forces in the finishing zone by changing the thickness of the Newtonian fluid layers and providing additional oscillating shear forces, which effectively reduced the unidirectional scratches.

(3) The surface roughness of the machined surface decreases monotonically in the working conditions of 0 ~ 45

μm and 0 ~350 Hz. The minimum surface roughness Sa value reduced from 123 nm to 17 nm compared to the sample without introducing vibration.

Author Contributions

Yan Gu and Bin Fu conducted this study, analyzed the data and drafted the manuscript. Yan Gu and Jieqiong Lin supervised this work. Xiuyuan Chen contributed to the literature review. Weidong Zhou, Bingjin Yu, Huibo Zhao, Zhen Li and Zisu Xu provided critical feedback and helped shape the research. All authors have read and agreed to the published version of the manuscript.

Funding

Data Availability

All data generated and analyzed during the study are included in this article.

Declarations

Code availability	Not applicable
Ethics approval	Not applicable
Consent to participate	Not applicable
Consent for publication	Not applicable
Conflicts of interest	The authors declare no competing interests.

Appendix A:

The derivation process of h^* :

First, substituting $\tan\theta = x / \sqrt{2Rh_{m0}}$ into $h_a = h_{m0} + x^2/2R$:

$$\begin{cases} h_a = h_{m0}\sec^2\theta \\ h^* = h_{m0}\sec^2\theta^* \end{cases} \quad (40)$$

Thus, the pressure gradient dP_d can be obtained as:

$$dP_d = 6\eta_1 U(\frac{h_a - h^*}{h_a^3})dx$$
$$= 6\eta_1 U(\frac{h_{m0}\sec^2\theta - h_{m0}\sec^2\theta^*}{h_{m0}^3\sec^6\theta})\sqrt{2Rh_{m0}}\sec^2\theta d\theta \quad (41)$$

Them, dimensionless pressure $\bar{P}_d$ is defined as:

$$\bar{P}_d = \frac{h_{m0}^2 P_d}{6\eta_1(U_1 + U_2)\sqrt{2Rh_{m0}}} \quad (42)$$

By combining Eqs. (41) and (42), the following equation is obtained:

$$\begin{cases} d\bar{P}_d = \cos^2\theta d\theta - \dfrac{\cos^4\theta d\theta}{\cos^2\theta^*} \\ \bar{P}_d = \dfrac{\theta}{2} + \dfrac{\sin 2\theta}{4} - \dfrac{1}{\cos^2\theta^*}(\dfrac{3}{8}\theta + \dfrac{\sin 2\theta}{32} + \dfrac{\sin 4\theta}{32}) + C \end{cases} \quad (43)$$

Finally, the Sommerfeld boundary conditions are adopted to obtain undetermined coefficients in Eq. (43):

$$\begin{cases} x = -\infty(\theta = -\dfrac{\pi}{2}), P = 0 \\ x = \infty(\theta = \dfrac{\pi}{2}), P = 0 \end{cases} \quad (44)$$

With this condition, the coefficients can be resolved as:

$$\begin{cases} C = \dfrac{\pi}{4} - \dfrac{1}{\cos^2\theta} \cdot \dfrac{3\pi}{16} \\ \cos^2\theta^* = \dfrac{3}{4} \end{cases} \quad (45)$$

Thus, the h^* is obtained:

$$h^* = h_{m0}\sec^2\theta^* = \frac{4}{3}h_{m0} \quad (46)$$

References

1. Otitoju TA, Okoye PU, Chen G, Li Y, Okoye MO, Li SX (2020) Advanced ceramic components: Materials, fabrication, and applications. J Ind Eng Chem 85: 34-65. https://doi.org/10.1016/j.jiec.2020.02.002

2. Goswami C, Patnaik A, Bhat IK, Singh T (2021) Mechanical physical and wear properties of some oxide ceramics for hip joint application: A short review. Materials Today: Proceedings 44(6): 4913-4918. https://doi.org/10.1016/j.matpr.2020.11.888

3. Belosludtsev A, Buinovskis D (2021) Significant increase of UV reflectivity of SiC galvanometer mirror scanners for the high-power laser applications. Opt Laser Technol 140: 107027. https://doi.org/10.1016/j.optlastec.2021.107027

4. Qiu Y, Zhu GZ, Min ZX, Liu Y (2021) Influence of ceramic substrate quality on CBGA assembly

reliability. Eng Fail Anal 123: 105316. https://doi.org/10.1016/j.engfailanal.2021.105316

5. Liang XH, Lin B, Liu XL (2020) Analysis of local features of engineering ceramics grinding surface. Measurement 151: 107205. https://doi.org/10.1016/j.measurement.2019.1072 05

6. Alam Z, Jha S (2017) Modeling of surface roughness in ball end magnetorheological finishing (BEMRF) process. Wear 374-375:54-62. https://doi.org/10.1016/j.wear.2016.11.039

7. Barman A, Das M (2017) Design and fabrication of a novel polishing tool for finishing freeform surfaces in magnetic field assisted finishing (MFAF) process. Precis Eng 49: 61-68. https://doi.org/10.1016/j.precisioneng.2017.01.010

8. Wang LY, Sun YL, Chen FY, Zhang GG, Zhang P, Zuo DW (2022) Experimental study on vibration-assisted magnetic abrasive finishing for internal blind cavity by bias external rotating magnetic pole. Precis Eng 74: 69-79.https://doi.org/10.1016/j.precisioneng.2021.11. 007

9. Bae JT, Kim HJ (2021) Finishing characteristics of Inconel alloy 625 bars in ultra-precision magnetic abrasive finishing using CNC machine center. J Mech Sci Technol 35(7): 2851-2859. https://doi.org/10.1007/s12206-021-0608-y

10. Xu JY, Zou YH (2021) Development of a new magnetic abrasive finishing process with renewable abrasive particles using the circulatory system. Precis Eng 72: 417-425. https://doi.org/10.1016/j.precisioneng.2021.06.004

11. Feng M, Wu YB, Wang YL, Zeng J, Bitoh T, Nomura M, Fujii T (2020) Investigation on the polishing of aspheric surfaces with a doughnut-shaped magnetic compound fluid (MCF) tool using an industrial robot. Precis En 61: 182-193. https://doi.org/10.1016/j.precisioneng.2019.09.018

12. Kumar M, Alok A, Kumar V, Das M (2021) Advanced abrasive-based nano-finishing processes: challenges, principles and recent applications, Mater Manuf Process 37(4):372-392. https://doi.org/10.1080/10426914.2021.2001 509

13. Wang YY, Zhang Y, Feng ZJ (2016) Analyzing and improving surface micro-grooves by dual-rotation magnetorheological finishing. Appl Surf Sci 360: 224-233. https://doi.org/10.1016/j.apsusc.2015.11.009

14. Paswan SK, Singh AK (2021) Theoretical analysis of a novel in-situ magnetorheological honing process for finishing the internal surface of tubular workpieces. Wear 476: 203698. https://doi.org/10.1016/j.wear.2021.203698

15. Jung BS, Jang K-I, Min B-K, Lee SJ, Seok JW (2009) Magnetorheological finishing process for hard materials using sintered iron-CNT compound abrasives. Int J Mach Tool Manu 49(5): 407-418. https://doi.org/10.1016/j.ijmachtools.2008.12.002

16. Lv BR, Lin B, Cao ZC, Li B,Wang GL(2022) A parallel 3-DOF micro-nano motion stage for vibration-assisted milling. Mech Mach Theory 173: 104854. https://doi.org/10.1016/j.mechmachtheory.2022.1 04854

17. Guo J, Jong HJH, Kang RK, Guo DM (2018) Novel localized vibration-assisted magnetic abrasive polishing method using loose abrasives for V-groove and Fresnel optics finishing. Opt Express 26(9): 11608-11619. https://doi.org/10.1364/OE.26.011608

18. Misra A, Pandey PM, Dixit US (2017) Modeling of material removal in ultrasonic assisted magnetic abrasive finishing process. Int J Mech Sci 131-132: 853-867. https://doi.org/10.1016/j.ijmecsci.2017.07.023

19. Jiang C, Huang JL, Jiang ZY, Qian DB, Hong XL (2019) Estimation of energy savings when adopting ultrasonic vibration-assisted magnetic compound fluid polishing. Int J Pr Eng Man-GT 8(1): 1-11. https://doi.org/10.1007/s40684-019-00167-5

20. Zhang FH, Yu XB, Zhang Y, Lin YY, Luan DR (2009) Experimental study on polishing characteristics of ultrasonic-magnetorheological compound finishing. Adv Mat Res 76-78: 235-239. https://doi.org/10.4028/www.scientific.net/AMR.7 6-78.235

21. Chen YR, Su HH, Qian N, He JY, Gu JQ, Xu JH, Ding K (2021) Ultrasonic vibration-assisted grinding of silicon carbide ceramics based on actual amplitude measurement: Grinding force and surface quality. Ceram Int 47(11): 15433-15441. https://doi.org/10.1016/j.ceramint.2021.02.109

22. Zhu ZH, Huang P,To S, Zhu LM, Zhu ZW(2023) Fast-tool-servo-controlled shear-thickening

micropolishing. Int J Mach Tool Manu 184: 103968. https://doi.org/10.1016/j.ijmachtools.2022.103968

23. Prabhu P, Rao M (2021) Investigations on piezo actuated micro XY stage for vibration-assisted micro milling. J Micromech Microeng 31(6): 065007. https://doi.org/10.1088/1361-6439/abfa7c

24. Chen XY, Gu Y, Lin JQ, Yi A, Kang MS, Cang XY (2020) Study on subsurface damage and surface quality of silicon carbide ceramic induced by a novel non-resonant vibration-assisted roll-type polishing. J Mater Process Tech 282: 116667. https://doi.org/10.1016/j.jmatprotec.2020.116667

25. Li YC, Zhou XQ, Liu Q (2021) Two-dimensional vibration actuated polishing of small surfaces by generating random-like Lissajous trajectories. Appl Optics 60(4): 851-863. https://doi.org/10.1364/AO.413073.

26. Gu Y, Kang MS, Lin JQ, Liu A, Fu B, Wan PH (2021) Non-resonant vibration-assisted magnetorheological finishing. Precis Eng 71: 263-281. https://doi.org/10.1016/j.precisioneng.2021.03.016

27. Kang MS, Gu Y, Lin JQ, Zhou XQ, Zhang S, Zhao HB, Li Z, Yu BJ, Fu B (2023). Material removal mechanism of non-resonant vibration-assisted magnetorheological finishing of Material Silicon carbide ceramics. Int J Mech Sci 242:107986. https://doi.org/10.1016/j.ijmecsci.2022.107986

28. Ghosh G, Sidpara A, Bandyopadhyay PP (2021) Theoretical analysis of magnetorheological finishing of HVOF sprayed WC-Co coating. Int J Mech Sci 207: 106629. https://doi.org/10.1016/j.ijmecsci.2021.106629

29. Ghosh G, Sidpara A, Bandyopadhyay PP (2021) Experimental and theoretical investigation into surface roughness and residual stress in magnetorheological finishing of OFHC copper. J Mater Process Tech 288: 116899. https://doi.org/10.1016/j.jmatprotec.2020.116899

30. Kumar M, Kumar A, Bharti RK, Yadav HNS, Das M (2021) A review on rheological properties of magnetorheological fluid for engineering components polishing. Materials Today: Proceedings 56(3): 6-12. https://doi.org/10.1016/j.matpr.2021.11.611

31. Shorey AB, Kordonski W, Tricard M (2004) Magnetorheological finishing of large and lightweight optics. QED Technologies Inc 5533: 99-107. https://doi.org/10.1117/12.559814

32. Chen MJ, Liu HN, Cheng J, Yu B, Fang Z (2017) Model of the material removal function and an experimental study on a magnetorheological finishing process using a small ball-end permanent-magnet polishing head. Appl Opt 56(19): 5573-5582. https://doi.org/10.1364/AO.56.005573

33. Xu JH, Li JY, Liu YM (2021) Investigation on the normal force in cluster magnetorheological-porous foam finishing process. Tribol Int 157: 106911. https://doi.org/10.1016/j.triboint.2021.106911

34. Zhang ZY, Geng K, Qiao GC, Zhang JH (2021) The heat flow coupling effect of laser-assisted magnetorheological polishing. Int J Adv Manuf Tech 114(1): 591-603. https://doi.org/10.1007/s00170-021-06880-3

35. Wang HJ, Zhang FH, Zhang Y, Luan DR (2007) Research on material removal of ultrasonic-magnetorheological compound finishing. Int J Machining and Machinability of Materials 2(1): 50-58. https://doi.org/10.1504/IJMMM.2007.012666

36. Zhai Q, Zhai WJ, Gao B (2021) Modeling of forces and material removal rate in ultrasound assisted magnetorheological polishing (UAMP) of sapphire. Colloid Surface A 628: 127272. https://doi.org/10.1016/j.colsurfa.2021.127272

37. Pan JS, Yan QS (2015) Material removal mechanism of cluster magnetorheological effect in plane polishing. Int J Adv Manuf Tech 81: 2017-2026. https://doi.org/10.1007/s00170-015-7332-7

38. Guo YF,Yin SH, Ohmori H, Li M, Chen FJ, Huang S (2022) A novel high efficiency magnetorheological polishing process excited by Halbach array magnetic field. Precis Eng 74: 175-185. https://doi.org/10.1016/j.precisioneng.2021.11.011

39. Aggarwal A , Singh AK (2021) Development of grinding wheel type magnetorheological finishing process for blind hole surfaces. Mater Manuf Process 36(4): 457-478. https://doi.org/10.1080/10426914.2020.1843666

40. Arora K, Singh AK (2021) Theoretical and experimental investigation on surface roughness of straight bevel gears using a novel magnetorheological finishing process. Wear 476: 203693. https://doi.org/10.1016/j.wear.2021.203693

41. Wang JJ, Yang Y, Guo P (2018) Effects of vibration trajectory on ductile-to-brittle transition in vibration cutting of single crystal silicon using a non-resonant tool. Procedia Cirp 71: 289-292. https://doi.org/10.1016/j.procir.2018.05.017

42. Fan W, Jin HX, Fu YC, Lin YY (2021) A type of symmetrical differential lever displacement amplification mechanism. Mech Ind 22: 5. https://doi.org/10.1051/meca/2021003

43. Gu Y, Duan XX, Lin JQ, Yi A, Kang MS, Jiang JJ, Zhou WD (2020) Design, analysis, and testing of a novel 2-DOF vibration-assisted polishing device driven by the piezoelectric actuators. Int J Adv Manuf Tech 111: 471-493. https://doi.org/10.1007/s00170-020-06043-w

44. Li XY, Li QK, Ye ZY, Zhang YF, Ye MH, Wang C (2021) Surface Roughness Tuning at Sub-Nanometer Level by Considering the Normal Stress Field in Magnetorheological Finishing. Micromachines 12(8): 997. https://doi.org/10.3390/mi12080997

45. Liu JB, Li XY, Zhang YF, Tian D, Ye MH, Wang C (2020) Predicting the Material Removal Rate (MRR) in surface Magnetorheological Finishing (MRF) based on the synergistic effect of pressure and shear stress. Appl Surf Sci 504: 144492. https://doi.org/10.1016/j.apsusc.2019.144492

46. Sidpara A, Das M, Jain VK (2009) Rheological Characterization of Magnetorheological Finishing Fluid. Mater Manuf Process 24(12): 1467-1478. http://dx.doi.org/10.1080/10426910903367410

47. Varela-Jimnez MI, Luna JLV, Corts-Ramrez JA, Song G (2015) Constitutive model for shear yield stress of magnetorheological fluid based on the concept of state transition. Smart Mater Struct 24(4): 045039. http://dx.doi.org/10.1088/0964-1726/24/4/045039

48. Garoosi F (2020) Presenting two new empirical models for calculating the effective dynamic viscosity and thermal conductivity of nanofluids. Powder Technol 366: 788-820. https://doi.org/10.1016/j.powtec.2020.03.032

49. Aboutalebi R, Eshaghi M,Hemmatian M, Sedaghati R (2021) Post-yield characteristics of magnetorheological fluids; from modelling to large-amplitude vibration analysis of sandwich plates using nonlinear finite element method. Aerosp Sci Technol 110: 106508. https://doi.org/10.1016/j.ast.2021.106508

50. Mohammadi N, Mahjoob MJ, Kaffashi B, Malakooti S (2010) An experimental evaluation of pre-yield and post-yield rheological models of magnetic field dependent smart materials. J Mech Sci Technol 24: 1829-1837. https://doi.org/10.1007/s12206-010-0607-x

51. Gong XL, Xu YG, Xuan SH, Guo CY, Zong LH (2012) The investigation on the nonlinearity of plasticine-like magnetorheological material under oscillatory shear rheometry. J Rheol 56(6): 1375-1391. https://doi.org/10.1122/1.4739263

52. Li WH, Du HJ, Chen G, Yeo SH (2001) Viscoelastic properties of MR fluids under oscillatory shear. Smart Mater Struct 4331: 333-342. https://doi.org/10.1117/12.432732

53. Shan L, Jia WP, Zhou M, Meng YG, Zhang XJ, Tian Y (2017) Frequency-independent viscoelasticity of carbonyl iron particle suspensions under a magnetic field. Smart Mater Struct 26: 054009. http://dx.doi.org/10.1088/1361-665x/26/5/054009

54. Kordonski WI, Jacobs SD (1996) Magnetorheological finishing. Int J Mod Phys B 10 (23n24): 2837-2848. https://doi.org/10.1142/S0217979296001288.

55. Gandhi F, Bullough WA (2016) On the Phenomenological Modeling of Electrorheological and Magnetorheological Fluid Preyield Behavior. J Intel Mat Syst Str 16(3): 237-248. https://doi.org/10.1177/1045389X05049649

56. Kamath GM, Werely NM (1997) Nonlinear Viscoelastic-Plastic Mechanisms-Based Model of an Electrorheological Damper. J Guid Control Dynam 20: 1125-1132. https://doi.org/10.2514/2.4167

57. Liu SW, Wang HX, Zhang QH, Hou J, Zhong B, Chen XH (2020) Regionalized modeling approach of tool influence function in magnetorheological finishing process for aspherical optics. Optik 206: 164368. https://doi.org/10.1016/j.ijleo.2020.164368

58. Feng YP, Su JS, Cheng HB (2016) Non-Newtonian hydrodynamic modeling of electrorheological finishing feature based on wheel-like finishing tool. J Intel Mat Syst Str 28(11): 1407-1414. http://dx.doi.org/10.1177/1045389x16672568

59. Zhang FD, Zhang XJ, Yu JC (2000) Mathematics model of magnetorheological finishing. In Advanced optical manufacturing and testing Technology. International Society for Optics and

Photonics 4231: 490-497. https://doi.org/10.1117/12.402796

60. Li WH, Zhou Y, Tian TF (2010) Viscoelastic properties of MR elastomers under harmonic loading. Rheol Acta 49: 733-740. https://doi.org/10.1007/s00397-010-0446-9

61. Zhang YF, Feng JB, Zhao YY, Rao MQ, Yin YH (2022) Towards understanding and restraining the mechanical relaxation effect in polishing silicon carbide with a detachable bonnet tool. Int J Mech Sci: 107962. https://doi.org/10.1016/j.ijmecsci.2022.107962